PNAS | RESEARCH ARTICLE | BIOCHEMISTRY

Molecular and structural basis of the dual regulation of the polycystin-2 ion channel by small-molecule ligands

Zhifei Wang[a,1], Mengying Chen[b,c,d,1], Qiang Su[b,c], Tiago D. C. Morais[a], Yan Wang[a], Elianna Nazginov[a], Akhilraj R. Pillai[a], Feng Qian[e], Yigong Shi[b,c,d], and Yong Yu[a,2]

Edited by Lily Jan, HHMI, University of California, San Francisco, CA; received September 21, 2023; accepted February 12, 2024

Mutations in the *PKD2* gene, which encodes the polycystin-2 (PC2, also called TRPP2) protein, lead to autosomal dominant polycystic kidney disease (ADPKD). As a member of the transient receptor potential (TRP) channel superfamily, PC2 functions as a non-selective cation channel. The activation and regulation of the PC2 channel are largely unknown, and direct binding of small-molecule ligands to this channel has not been reported. In this work, we found that most known small-molecule agonists of the mucolipin TRP (TRPML) channels inhibit the activity of the PC2_F604P, a gain-of-function mutant of the PC2 channel. However, two of them, ML-SA1 and SF-51, have dual regulatory effects, with low concentration further activating PC2_F604P, and high concentration leading to inactivation of the channel. With two cryo-electron microscopy (cryo-EM) structures, a molecular docking model, and mutagenesis results, we identified two distinct binding sites of ML-SA1 in PC2_F604P that are responsible for activation and inactivation, respectively. These results provide structural and functional insights into how ligands regulate PC2 channel function through unusual mechanisms and may help design compounds that are more efficient and specific in regulating the PC2 channel and potentially also for ADPKD treatment.

ion channel | transient receptor potential channel | ligand | polycystic kidney disease | cryo-EM structure

Autosomal dominant polycystic kidney disease (ADPKD), one of the most common genetic diseases in humans, affects 1 in every 400-1,000 individuals and leads to end-stage renal disease in half of the patients (1, 2). ADPKD is caused by mutations in the *PKD1* or *PKD2* genes, encoding integral membrane proteins polycystin-1 (PC1, or PKD1) and polycystin-2 (PC2, PKD2, or TRPP2) proteins, respectively (3, 4). PC1 and PC2 form a complex (5–8) and function as a non-selective cation channel (9–11). Besides interacting with PC1, PC2 also forms a homotetrameric non-selective cation channel (12, 13).

PC2 belongs to the transient receptor potential (TRP) cation channel superfamily and the polycystin subfamily (TRPP). TRP channels are directly involved in many sensory perceptions and regulated by a broad range of stimuli (14–17). They are connected to numerous human diseases and serve as common drug targets (14–17). All TRP proteins have similar structural features such as six transmembrane segments (S1–S6) and intracellular N and C termini (18). Recently reported cryo-electron microscopy (cryo-EM) structures of the PC2 tetramer have significantly enhanced our understanding of this channel (19–21). Like other TRP proteins, the first four transmembrane segments (S1–S4) of each PC2 subunit form a voltage-sensor domain (VSD)-like structure and stay in the periphery, resembling the VSD in voltage-gated ion channels. S5 and S6, as well as the linker (pore loop, P-loop) between them, form the pore domain. The pore domains from the four subunits assemble into a four-fold symmetrical structure to form an ion-conducting pathway (pore) in the middle. The P-loops define the extracellular end of the pore and form a selectivity filter, which determines channel permeability and ion selectivity. The bottom part of the pore contains the gate, which is formed by the side chains of F677 and N681 in S6 (19–21). The S1–S4 and pore domains assemble in a domain-swapped arrangement, similar to that in the classical voltage-gated channels (19–21).

Within the TRP family, TRPP and mucolipin TRP (TRPML) proteins are most closely related to each other. The reported cryo-electron microscopy (cryo-EM) structures of TRPP and TRPML channels also share high similarity (21–25). A unique structural feature these proteins have is the large extracellular loop that links the first and the second transmembrane domains. This loop has a highly ordered structure in cryo-EM structures of TRPP and TRPML proteins, containing mainly beta sheets and some alpha helices. It has been called the polycystin–mucolipin domain (PMD) (26), polycystin domain (21), or tetragonal opening for polycystins (TOP) domain (20). Here, we will call it the TOP domain since this name suggests its location (above the channel pore) in the structures.

Significance

Mutations in the polycystin-2 (PC2, also known as TRPP2) ion channel protein lead to autosomal dominant polycystic kidney disease (ADPKD), one of the most common genetic diseases in humans. The activation mechanism of this channel is unknown, and limited tools are available for its functional study. In this work, we reported a group of small-molecule ligands that can regulate the function of a gain-of-function PC2 mutant and identified two binding sites of the ligand ML-SA1 in PC2 structure that correspond to activation and inactivation of the channel, respectively. This work found useful tools for functional studies of PC2, provided insights into its structure, and will help design new ligands for studying this channel and potentially ADPKD treatment.

Author contributions: F.Q., Y.S., and Y.Y. designed research; Z.W., M.C., Q.S., T.D.C.M., Y.W., E.N., and A.R.P. performed research; Z.W., M.C., Q.S., and Y.Y. analyzed data; Y.Y. conceived the project; and Z.W., M.C., Q.S., and Y.Y. wrote the paper.

The authors declare no competing interest.

This article is a PNAS Direct Submission.

[1] Z.W. and M.C. contributed equally to this work.

[2] To whom correspondence may be addressed. Email: yuy2@stjohns.edu.

This article contains supporting information online at https://www.pnas.org/lookup/suppl/doi:10.1073/pnas.2316230121/-/DCSupplemental.

The TOP domains from four subunits interact and assemble into a donut-like structure with a large hole in the center. In the cryo-EM structures of PC2, the TOP domain forms a direct interaction with the outer pore and the linker between S3 and S4, suggesting a possible role of it in channel gating (19–21).

The in vivo functions of the PC1 and PC2 and how their mutations lead to ADPKD are still elusive. One of the biggest challenges is the lack of a reliable in vivo or in vitro activation mechanism for studying the PC2 and PC1/PC2 channels. To help this, we previously developed gain-of-function (GOF) mutants of the PC2 and PC1/PC2 channels, which, applied in multiple labs, provided capable platforms for function analysis (9, 27–30). PC2_F604P, a GOF mutant of the PC2 homomeric channel, which carries the mutation F604P in S5, gave rise to robust currents when expressed in *Xenopus laevis* oocytes (28). When expressed in zebrafish embryos, PC2_F604P, compared to the wild-type (WT) PC2, better rescued the PC2 downregulation–induced morphological abnormalities (27, 28). The cryo-EM structure of PC2_F604P shows that the F604P mutation destabilizes the interaction between S5 and S6 and leads to the conversion of a π-helix turn in the middle of S6 to an alpha helix. Consequently, this results in twisting and rotation of the bottom half of S6 which opens the lower gate of the channel (27). Similar conformational changes in the pore happen in the gating process of some other TRP channels, including another TRPP member polycystin-2L1 (PC2L1, also called PCL or TRPP3) (31, 32). Thus, the F604P mutation-induced channel opening may mimic a natural gating process.

Many small molecules, either natural products or synthetic compounds, have been found to bind ion channels as agonists and antagonists. They are not only useful in studying channel function but also have potential clinical applications. Previously, many ligands have been identified and well studied for other TRP channels (33). As for PC2, although some lipid molecules like phosphatidic acid (PA), phosphatidylinositol 4,5-bisphosphate (PIP2), and cholesterol have been suggested to bind to this channel (19, 34), it is not known how they modulate PC2 function. Identifying small molecules that can gate or regulate the PC2 channel will bring valuable tools to the field and significantly speed up its study. In this work, after testing a series of TRPML agonists on WT PC2 and the GOF PC2_F604P, we found most of them inhibit the activity of PC2_F604P, while two of them, ML-SA1 and SF-51, further activate the channel at low concentrations and inactivate it at higher concentrations. Using cryo-EM, molecular docking, and mutagenesis methods, we dissected how the binding of ML-SA1 at two distinct sites leads to opposite effects on PC2_F604P.

Results

TRPML Agonists Regulate the Activity of PC2_F604P. Previously, multiple small molecule agonists of TRPML channels have been identified (35–38). Since TRPML proteins share high structural similarity with TRPP proteins, we focused on these TRPML agonists when looking for small-molecule ligands of PC2. In this study, we tested 15 of them [their International Union of the Pure and Applied Chemistry (IUPAC) names are listed in *SI Appendix*, Table S1]. In our test, these molecules were applied to the extracellular side of the WT PC2 and the PC2_F604P channels expressed in *Xenopus* oocytes. When 10 or 100 μM of molecules were applied, although none of them activates the WT PC2, thirteen of them (MK6-83, ML2-SA1, SF-21, SF-22, SF-23, SF-24, SF-31, SF-32, SF-33, SF-41, SF-71, SN-2, and rapamycin) caused significant inhibition to the channel activity of PC2_F604P (*SI Appendix*, Table S2 and Fig. S1). In 100 μM, these molecules inhibited channel current from ~30% to ~80% at +80 mV. In contrast, applying 10 μM or 100 μM ML-SA1, a synthetic agonist of all three TRPML channels (35), further activated the PC2_F604P channel, leading to ~70% increases of currents at +80 mV in these initial tests (*SI Appendix*, Table S2). Application of a TRPML3 activator, SF-51 (36), also led to a smaller increase of PC2_F604P current (*SI Appendix*, Table S2). It is worth noticing that ML-SA1 is a structural analog of SF-51, and the two molecules share a very similar structure (35, 36). These results indicate that TRPML ligands can bind and regulate the PC2_F604P channel. To investigate the molecular mechanisms of the regulation, we next focused on the activation effect of ML-SA1 on PC2_F604P.

ML-SA1 Further Activates the PC2_F604P. In a bath solution containing 100 mM Na^+ and 2 mM Ca^{2+} as cations, applying 20 μM ML-SA1 at the extracellular side roughly doubled the outward current of PC2_F604P at +80 mV (Fig. 1 *A* and *B*). The EC_{50} of ML-SA1 for activating PC2_F604P is 5.2 μM (Fig. 1*C*). We previously found that the inward current of PC2_F604P was blocked by divalent ions Ca^{2+} and Mg^{2+} at the extracellular side (28). This blocking was not affected by ML-SA1 treatment (Fig. 1*B* and *SI Appendix*, Fig. S2). The activation by ML-SA1 is not Ca^{2+}-dependent either since a similar activating effect was found when Ca^{2+} was removed from the bath solution (Fig. 1*D*). In similar tests, ML-SA1 did not activate WT PC2 and had no effect on the current of another GOF mutant PC2_AA (L677A/N681A) (9) (*SI Appendix*, Fig. S3). The AA mutation opens the channel by removing the bulky side chains at the gate of the channel, which is different from the GOF mechanism of the F604P mutant. Therefore, the structural disparities between the pore domains of PC2_AA and PC2_F604P may explain why ML-SA1 has no effect on PC2_AA.

The Ca^{2+} permeability property of the PC2 channel, a critical feature for PC2's potential physiology functions, remains largely elusive (9, 39, 40). To test whether the ML-SA1 activation increases the Ca^{2+} permeability of PC2_F604P, we first recorded currents in a solution containing 70 mM Ca-gluconate in the absence and presence of 20 μM ML-SA1. Replacing all other cations with 70 mM Ca^{2+} helps to promote Ca^{2+} influx. At the same time, replacing Cl^- with gluconate helps to avoid the current contamination from endogenously expressed calcium-activated chloride channel (CACC) in oocytes (41–43) since gluconate is not permeable through CACC. In the absence of ML-SA1, PC2_F604P current recorded in 70 mM Ca-gluconate (Fig. 1*E*) shows no inward current at negative voltages (Fig. 1*B*), suggesting no Ca^{2+} influx. This result is consistent with our previous observation that PC2_F604P has no obvious Ca^{2+} permeability (9). Adding 20 μM ML-SA1 in the bath led to a significantly larger outward current at positive voltages due to ML-SA1 activation (Fig. 1*E*). However, there is no obvious increase of the inward current at negative voltages (Fig. 1*E*). These results suggest that if the ML-SA1-treated PC2_F604P has Ca^{2+} permeability, it is still too small to give recordable Ca^{2+} influx.

The activation of CACC can be used to monitor the trace amount of Ca^{2+} influx through low Ca^{2+}-permeable channels (9). To further test whether ML-SA1-activated PC2_F604P has gained a small amount of Ca^{2+} permeability, we next switch to a bath solution containing 70 mM $CaCl_2$ with 20 μM ML-SA1. In this solution, if CACC is activated by Ca^{2+} influx through ML-SA1-activated PC604P, we should be able to record CACC currents. In our tests, we indeed observed that both inward and

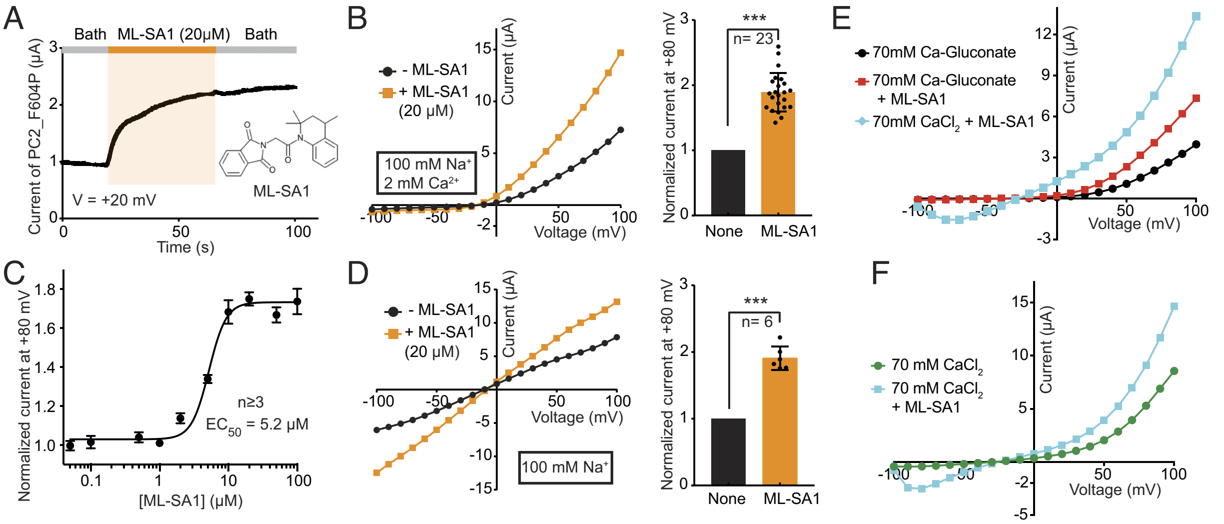

Fig. 1. ML-SA1 further activates the GOF PC2_F604P channel. (*A*) Representative gap-free recording at +20 mV shows that ML-SA1 activates PC2_F604P in a bath solution containing 100 mM Na^+ and 2 mM Ca^{2+}. The structure of the ML-SA1 molecule is shown as an insertion. (*B*) Representative I–V curves (*Left*) and scatter plot and bar graph (*Right*) show currents of PC2_F604P before and after applying 20 μM ML-SA1 in a bath solution containing 100 mM Na^+ and 2 mM Ca^{2+}. In the scatter plot and bar graph, the current at +80 mV of each oocyte was normalized to its current before applying ML-SA1. Data are presented as mean ± SD in bar graphs here and those in the other figures (****P* < 0.001, Student's *t* test). (*C*) Concentration–response curve of the effect of ML-SA1 on increasing the current of PC2_F604P at +80 mV when recorded in 100 mM Na^+/2 mM Ca^{2+} solution. Data were collected when currents reached the peak seconds after the ML-SA1 application. (*D*) Same as in *B* except that the currents were recorded in a bath solution without Ca^{2+}. (*E*) Representative I–V curves of PC2_F604P, recorded before and after treatment of 20 μM ML-SA1 in 70 mM Ca-gluconate, and then switched to 70 mM $CaCl_2$ with 20 μM ML-SA1. (*F*) Representative I–V curves of PC2_F604P recorded in 70 mM $CaCl_2$ before and after treatment of 20 μM ML-SA1.

outward currents became significantly larger (Fig. 1*E*). The I–V curve at negative voltage shows an unusual trough at strong hyperpolarization, a characteristic of the CACC current in this ionic condition (9), suggesting CACC was indeed activated by Ca^{2+} influx. The trace amount of Ca^{2+} influx through PC2_F604P was induced by ML-SA1 activation, since when recorded in 70 mM $CaCl_2$ solution, the CACC current component was only seen after applying ML-SA1 (Fig. 1*F*). Thus, these results suggest that ML-SA1-activated PC2_F604P channel gains some Ca^{2+} permeability. Although the Ca^{2+} influx is too small to be directly recorded, it is large enough to activate CACC (Fig. 1*E*).

ML-SA1 Likely Binds to PC2_F604P at a Site Similar to Its Binding Site in TRPML1. We next explored the binding site of ML-SA1 in PC2_F604P. In the reported cryo-EM structures of the TRPML1/ML-SA1 complex, the ML-SA1 binds in a hydrophobic cavity formed by several aromatic and hydrophobic residues in pore helix 1 (PH1), helices S5 and S6, and helix S6 of a neighboring subunit (23, 44, 45) (Fig. 2 *A* and *B*). The binding sites of agonist temsirolimus (a rapamycin analog) (44) and antagonist ML-SI3 (46) in TRPML1, and ML-SA1 in TRPML3 (22), also fall into the same cavity. Moreover, lipids and several blockers have been reported to bind at similar positions in TRPV1 and a model bacterial voltage-gated Ca channel CavAb (47, 48). Thus, this hydrophobic cavity serves as a common site for regulating TRP channel function. We wondered whether ML-SA1 also binds to a similar site in PC2_F604P.

The sequence alignment between PC2 and TRPML1 in the S5-pore-S6 region shows that most of the residues that play key roles in ML-SA1 binding in TRPML1, including F465 and I468 of PH1; F428, V432, and Y436 of S5; F505 and F513 of S6; and Y507 of S6 in the neighboring subunit, are either identical or conserved between the two proteins (Fig. 2*A*). These key residues are also structurally conserved in WT PC2, as seen when aligning the cryo-EM structures of TRPML1 (22) with the WT PC2 (21) (Fig. 2 *C*, *Left*). Even the non-conserved residue Y499 of TRPML1, which is a threonine (T662) in PC2 (Fig. 2*A*), aligned well with the latter in the structures (Fig. 2 *C*, *Left*). In contrast, in PC2_F604P (27), although most of these residues are also structurally similar to those in TRPML1, the side chain positions of two key residues at the bottom of the ML-SA1 binding cavity in TRPML1, F513 on S6, and Y507 on S6 in the neighboring subunit, are significantly different in PC2_F604P (Fig. 2 *C*, *Right*). In PC2_F604P, the aligned residue F676 stays much further to the binding cavity and the side chain of F670 flips away from it (Fig. 2 *C*, *Right*). These changes are caused by the F604P mutation-induced rotation in the bottom half of S6 (27). Thus, based on the structures, it appears that ML-SA1 should bind more stably to WT PC2 than to PC2_F604P. In contrast, our results show that PC2_F604P, but not the WT PC2, is activated by ML-SA1. So, it is possible that either ML-SA1 does bind to the WT PC2 but cannot activate it, or the conformational changes at the bottom of the binding cavity in PC2_F604P promote the accessing and binding of ML-SA1.

To confirm the binding of ML-SA1 in this cavity, we generated four individual mutations based on the sequence alignment between PC2 and TRPML1: F608A in S5, F637A in PH1, F676A in S6, and F670A in the neighboring S6, and tested the mutants' responses to ML-SA1 treatment. The results of F608A and F637A are not conclusive since both mutations abolished PC2_F604P channel activity (*SI Appendix*, Fig. S4). Consistently, the corresponding mutations Y436A and F465A in TRPML1 also led to a dead channel (23). The other two mutations, F670A and F676A, did not affect PC2_F604P current, but completely abolished the activation of ML-SA1 (Fig. 2 *D* and *E*). The effect of F676A on ML-SA1 activation is consistent with that of the corresponding mutations F513A in TRPML1 (23) and F497A in TRPML3 (22). Thus, although we could not rule out the possibility that the effects of F670A and F676A are indirect to ML-SA1 binding or activation, considering the sequence and structural conservation of this binding cavity between PC2 and TRPML and the similar effects of

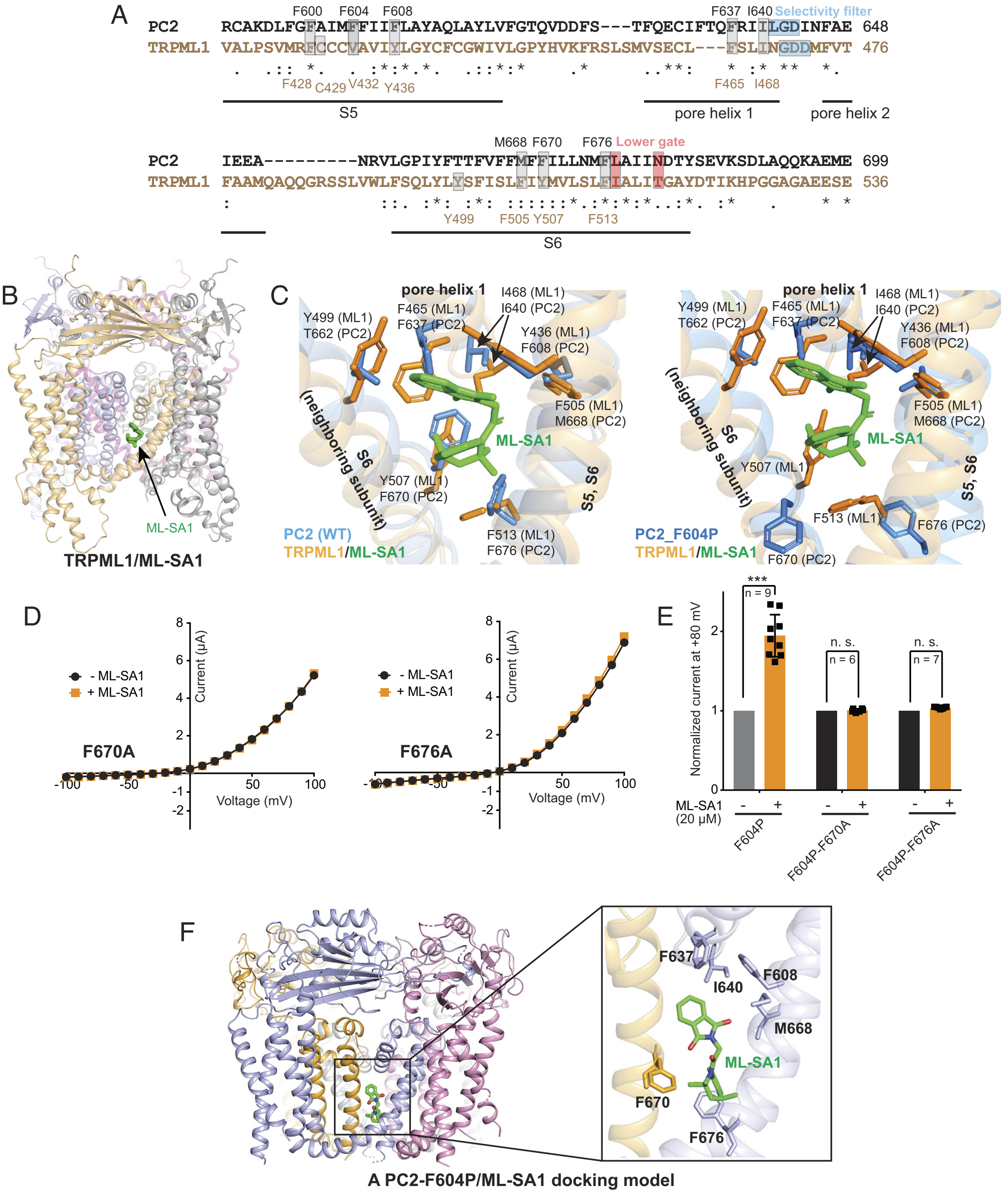

Fig. 2. The activating binding site of ML-SA1 in PC2_F604P. (*A*) Sequence alignment shows conservation between PC2 and TRPML1 at the indicated regions. Gray boxes indicate the key residues at the ML-SA1 binding site in TRPML1 (23) and the aligned residues in PC2. Blue and pink boxes indicate the selectivity filter and lower gate, respectively. Asterisk: identical; double dots: conserved; single dot: similar. (*B*) Cryo-EM structure of the human TRPML1/ML-SA1 complex (PDB #5WJ9) (23). (*C*) Structural alignment between TRPML1/ML-SA1 and WT PC2 (PDB #5T4D) (21) (*Left*), and TRPML1/ML-SA1 and PC2_F604P (PDB #6D1W) (27) (*Right*). Side chains of key residues in the ML-SA1 binding site in TRPML1 and their aligned residues in PC2 are shown. (*D* and *E*) Representative I–V curves (*D*) and scatter plots and bar graphs (*E*) show the currents of PC2_F604P-F670A and PC2_F604P-F676A mutants before and after 20 μM ML-SA1 treatment. Currents at +80 mV are shown in bar graphs and were normalized to currents before ML-SA1 treatment (***$P < 0.001$, n.s.: no significance, Student's *t* test). (*F*) A docking model showing a ML-SA1 molecule docked in a cavity of PC2_F604P that matches the ML-SA1 binding site in TRPML1. In the zoomed-in picture (*Right*), key residues in PC2_F604P that are aligned to those involved in ML-SA1 binding in TRPML1 are shown.

these mutations, the results strongly suggest that F670 and F676 are directly involved in the binding of ML-SA1 in PC2_F604P. Interestingly, F670 and F676 are the two amino acids that show significant structural differences between the WT PC2 and PC2_F604P (Fig. 2*C*). Thus, it is possible that the positions of their side chains in PC2_F604P favorite ML-SA1 binding, thereby leading to its activation. This point is further suggested by the docking model shown below.

To further investigate the binding of ML-SA1 in PC2_F604P, we generated a molecular model of the PC2_F604P/ML-SA1 complex by conducting ligand docking with the cryo-EM structure of PC2_F604P (21). In 47 out of the 50 docking runs we conducted, the ML-SA1 molecule ended up binding to the same cavity that ML-SA1 binds to TRPML1 (23). A model of ML-SA1 binding in PC2_F604P with the lowest free energy is shown in Fig. 2*F*. The key residues mentioned above are nicely surrounding ML-SA1 in our model (Fig. 2*F*). We noticed that the ML-SA1 molecule in most (43 out of 47) of docking model showed extended structure instead of the folded structure seen in the cryo-EM structure of TRPML1/ML-SA1 (23). The extended structure of ML-SA1 seems necessary in our model to reach F670 and F676, which are located further from the binding cavity compared to the aligned residues in the TRPML1 structure (Fig. 2 *C* and *F*). The docking results further confirm that ML-SA1 binds in the cavity formed by PH1, S5, S6, and neighboring S6 in PC2_F604P to activate the channel.

Inhibitors SF-33 and SF-71 May Bind at the Same Site as ML-SA1 in PC2_F604P. We next investigated the inhibition of SF-33 and SF-71, the two most efficient molecules that inhibit PC2_F604P current (*SI Appendix*, Table S2). In a bath solution containing 100 mM Na^+ and 2 mM Ca^{2+}, 20 μM SF-33 or SF-71 causes about 50% inhibition of the outward current of PC2_F604P at +80 mV (Fig. 3 *A* and *C*). The IC_{50} values of the two molecules are 16.9 μM and 6 μM, respectively (Fig. 3 *B* and *D*). A synthetic antagonist ML-SI3 was previously shown to bind at the same site as ML-SA1 in TRPML1 and thus directly compete with ML-SA1 in its binding to inhibit channel activity (46). Here, we found that applying either SF-33 or SF-71 after ML-SA1 application inhibited ML-SA-activated PC2_F604P (Fig. 3*E*). Similarly, ML-SA1 application also reversed the inhibition caused by either SF-33 or SF-71 (Fig. 3*F*). These results indicate that SF-33 and SF-71 may also bind to the same site as ML-SA1 and can compete with the latter. To confirm it, we tested the effects of these two inhibitors on the PC2_F604P channel carrying the ML-SA1-binding site mutations F670A and F676A. The results show that the inhibition of SF-33 and SF-71 is greatly reduced by these two mutations (Fig. 3*G*, compared to Fig. 3 *A* and *C*). Although mild inhibition was still seen when 100 μM inhibitors were applied on the F676A mutant, almost no inhibition was seen when applying 20 μM inhibitors on both mutants (Fig. 3*G* and *SI Appendix*, Fig. S5). These results strongly suggest that SF-33 and SF-71 also bind to the same site as ML-SA1 in PC2_F604P.

The Dual Effects of the "Activators": High-Concentration-Mediated Inactivation. During our study of ML-SA1 activation, we noticed that when applied 20 μM ML-SA1 to activate PC2_F604P first, the subsequent application of 100 μM ML-SA1 resulted in no further activation but rather a reduction in current (Fig. 4 *A* and *B*). Since 20 μM ML-SA1 has reached the

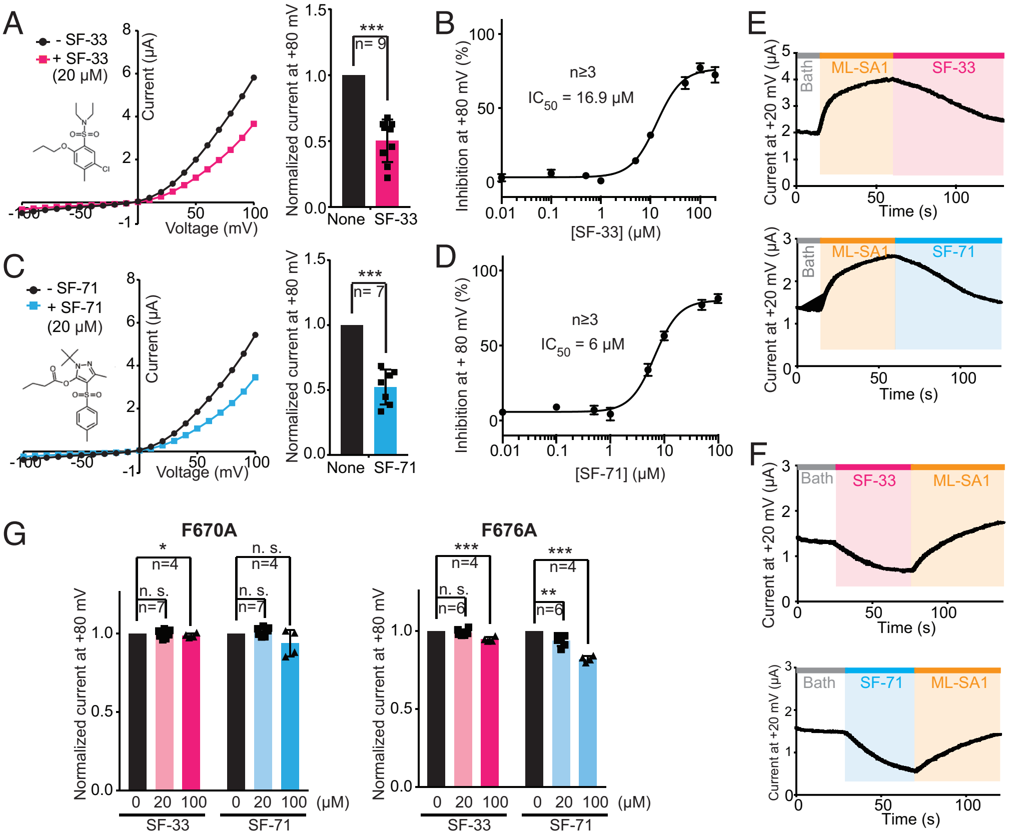

Fig. 3. SF-33 and SF-71 may bind to the same site as ML-SA1 to inhibit PC2_F604P current. (*A*) Representative I–V curves (*Left*) and scatter plot and bar graph (*Right*) show currents of PC2_F604P before and after applying 20 μM SF-33 in a bath solution containing 100 mM Na^+ and 2 mM Ca^{2+}. Normalized currents at +80 mV are shown in the scatter plot and bar graph (***$P < 0.001$, Student's *t* test). The structures of SF-33 is shown as insertion. (*B*) Concentration–response curves of the effect of SF-33 on inhibiting the current of PC2_F604P at +80 mV. (*C* and *D*) Same as in *A* and *B* except that 20 μM SF-71 was applied instead of SF-33. (*E* and *F*) Representative gap-free recording at +20 mV showing applying SF-33 or SF-71 removed the activation effect of ML-SA1 (*E*) and applying ML-SA1 also removed inhibition of SF-33 or SF-71 (*F*). (*G*) Scatter plots and bar graphs show the inhibitory effects of SF-33 and SF-71 at the indicated concentration on the PC2_F604P channel carrying either F670A (*Left*) or F676A (*Right*) mutation. Normalized currents at +80 mV are shown in bar graphs (*$P < 0.05$, **$P < 0.01$, ***$P < 0.001$, n.s.: no significance, Student's *t* test). Representative I–V curves are shown in *SI Appendix*, Fig. S5.

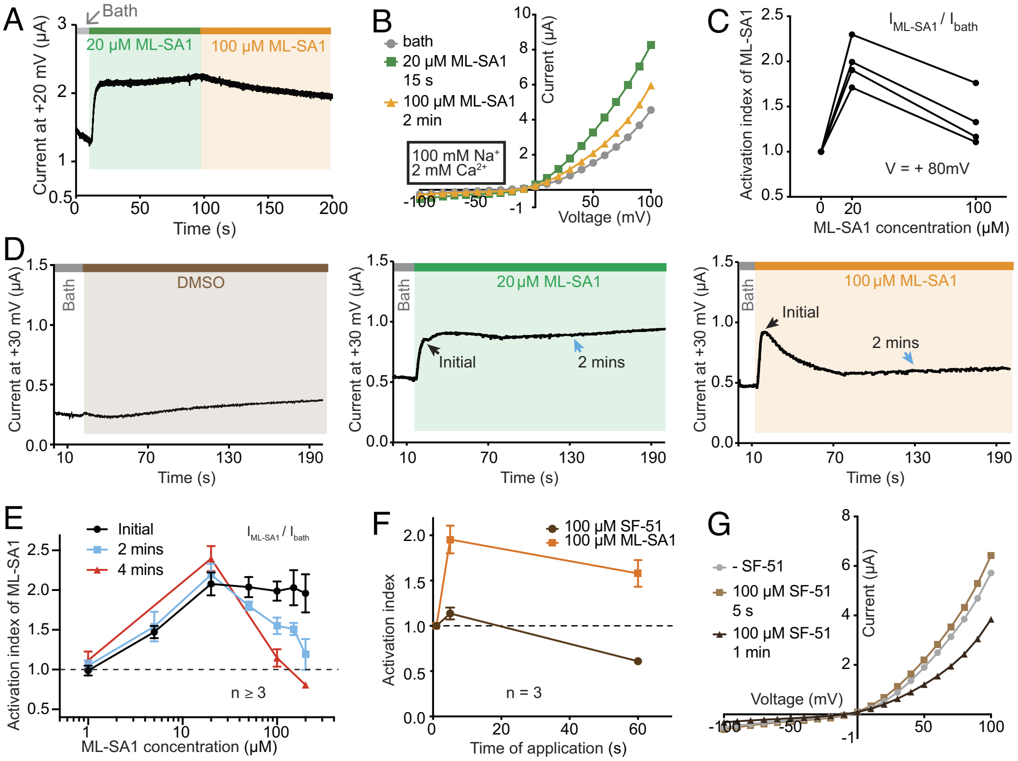

Fig. 4. High concentrations of ML-SA1 and SF-51 inhibit the activity of the PC2-F604P. (*A* and *B*) Representative gap-free recording at +20 mV (*A*) and I–V curve (*B*) of the PC2_F604P current, showing the activation after applying 20 μM ML-SA1 and the inhibition after applying 100 μM ML-SA1. (*C*) The plot of the activation index (ratio of current at +80 mV after ML-SA1 application vs. current before application, $I_{ML\text{-}SA1}/I_{bath}$) of ML-SA1 at 20 and 100 μM, showing the initial activation after applying 20 μM ML-SA1 and the inhibition after further applying 100 μM ML-SA1 for 2 min. Data from four individual oocytes are shown. (*D*) Gap-free recording of PC2_F604P at +20 mV showing the effects of applying 20 μM (*Middle*) or 100 μM (*Right*) ML-SA1 for a relatively long time. Applying 100 μM ML-SA1 led to a sharp increase followed by a gradual decrease in the current. The current at the initial activation peak and after 2 min application, which were used in generating curves in *E*, are indicated. DMSO, which was used to help dissolve ML-SA1, was tested as negative control (*Left*). (*E*) Plot of the activation index of ML-SA1 at the "initial" activation peak, 2 min, and 4 min after applying indicated concentrations of ML-SA1, showing that concentrations above 20 μM led to inhibition after the initial activation. (*F*) Activation indexes of 100 μM ML-SA1 or 100 μM SF-51, measured at around 5 s when the current reached the peaks and 1 min after application, showing that SF-51 caused stronger inhibition than ML-SA1. (*G*) Representative I–V curves showing the current of PC2_F604P before and after applying 100 μM SF-51 for 5 s or 1 min.

saturated concentration for PC2_F604P activation (Fig. 1*C*, where the peak currents right after ML-SA1 application were recorded), it is reasonable that 100 μM ML-SA1 did not induce a bigger current. However, the reduction in current suggests that inactivation or desensitization occurred after the application of 100 μM of ML-SA1. To better describe the dual effects of ML-SA1 on PC2_F604P current, we divided the currents of PC2_F604P after the application of ML-SA1 (20 or 100 μM) ($I_{ML\text{-}SA1}$) by the current before ML-SA1 appellation (I_{bath}) and named the ratio ($I_{ML\text{-}SA1}/I_{bath}$) "activation index." Plotting the activation index of each oocyte gives us a clear view of how the application of 100 μM ML-SA1 led to significant inactivation/desensitization of PC2_F604P that has been activated by 20 μM ML-SA1 (Fig. 4*C*).

Applying 100 μM ML-SA1 directly to PC2_F604P without the pre-treatment of 20 μM ML-SA1 led to a sharp initial increase followed immediately by a gradual decrease of the current (Fig. 4 *D*, *Right*). The current dropped back to almost the pre-treatment level after about 1 min (Fig. 4 *D*, *Right*). The reduction did not happen after a long-term application of 20 μM ML-SA1 (Fig. 4 *D*, *Middle*). The fact that this inactivation/desensitization never occurred when applying 20 μM ML-SA1 (Figs. 1*A* and 4 *A* and *D*) suggests that the reduction of current in 100 μM MLL-SA1 is caused by inactivation, instead of desensitization. Moreover, these results suggest that there may be a second inhibitory binding site of ML-SA1 in PC2_F604P. This second site probably has a low affinity to ML-SA1, so the binding only happens when ML-SA1 concentration is high enough. When 100 μM ML-SA1 is applied, ML-SA1 binds to the first activation site in the S5-PH1-S6 cavity to activate PC2_F604P, then after ML-SA1 further binds to the secondary low-affinity inhibitory site, the channel is inactivated. In contrast, when 20 μM ML-SA1 is applied, only the activation site is occupied by the ligand, and the channel was activated and stays at the activation state.

To explore the necessary concentration for ML-SA1-induced inactivation, we applied ML-SA1 with a series of concentrations from 1 μM to 200 μM and recorded the current at the activation peak (initial) and current after 2 min application Fig. 4*D* and calculated the activation index for each concentration at these two time points. The results show that the initial activation index reaches saturation at around 20 μM and stays stable even when higher concentrations of ML-SA1 were applied (Fig. 4*E*, black line). The activation index at 2 min, however, starts dropping when concentration is higher than 20 μM (Fig. 4*E*, blue line), indicating ML-SA1 starts binding to the inhibitory site when concentration is more than 20 μM. In most of the cases, we noticed that the inactivation caused by high concentrations of ML-SA1 usually only partially eliminates the increased current caused by ML-SA1 activation (Fig. 4*E*). However, when we pushed the test to 4 min after ML-SA1 application, applying 200 μM ML-SA1 led the current of PC2_F604P dropped to even smaller than the current before applying ML-SA1 (Fig. 4*E*, red line), suggesting the inactivation does not only offset the initial

ML-SA1 activation, but also inhibits the PC2 activity generated by the GOF mutant. This is clearer in the case of another PC2_F604P activator SF-51. When applying 100 μM SF-51, there was only a small initial increase of current within several seconds followed by a faster decrease compared to that in the case of ML-SA1 treatment (Fig. 4*F*). At 1 min after application, the current has become about 40% smaller than the original PC2_F604P current (Fig. 4 *F* and *G*). In this sense, the relatively small activation effect of SF-51 seen in our experiments may just be caused by its fast and strong inactivation effect, as the latter can hide most of the initial activation. The fact that applying 200 μM ML-SA1 for 4 min or 100 μM SF-51 for 1 min made the current of PC2_F604P become even smaller than its original current before treatment further suggests that inactivation, instead of desensitization, happened in these treatments.

ML-SA1 Binds to the TOP/Outer Pore Site of PC2_F604P. To better understand the molecular mechanism of the dual regulation of PC2_F604P by ML-SA1, we went to solve the cryo-EM structures of the PC2_F604P with or without ML-SA1, using a truncated PC2_F604P protein containing the fragment Pro185-Lys719. First, we tried to resolve the structure in the presence of 20 μM ML-SA1. However, no clear densities that accounted for ML-SA1 were found in the EM map. After increasing the concentration of ML-SA1 to 200 μM, we were able to resolve a structure of the PC2_F604P/ML-SA1 complex with an overall resolution of 2.96 Å. At the same time, we have also resolved a structure of PC2_F604P in the absence of ML-SA1 with an overall resolution of 2.99 Å (Fig. 5*A* and *SI Appendix*, Figs. S6–S9 and Table S3).

Surprisingly, in the structure resolved in the presence of ML-SA1, we could not find the ML-SA1 molecule at the above-discussed PH1-S5-S6 site. However, unambiguous non-protein densities show up at a space formed by the TOP domain, S4 of one subunit, and the outer pore region of a neighboring subunit (Fig. 5 *A* and *B*). This density is short and fat and ML-SA1 molecule fits well into it. Thus, we tentatively assigned this density, which is almost equivalent in each monomer under C1 symmetry, to the ML-SA1 molecule (Fig. 5 *A* and *B* and *SI Appendix*, Fig. S9*B*). Mutagenesis data shown below confirmed the assignment of ML-SA1 to this density. Therefore, this structure is referred to as "PC2_F604P_ML-SA1." In our structure resolved in the absence of ML-SA1, a density was also observed at a similar position. However, this density is larger and elongated, which is obviously different from that in the PC2_F604P_ML-SA1 structure. A phospholipid-like molecule can be accommodated to this density (*SI Appendix*, Fig. S9*A* and Fig. 5*C*). Thus, we refer to this structure as "PC2_F604P_lipid." Both densities are not seen in the previously reported PC2_F604P structure (referred to as "PC2_F604P_apo" here) (27) (Fig. 5*D*).

Further analysis of this ML-SA1 binding site shows that although the binding pocket is mainly hydrophobic (Fig. 5*E*), the key residues that are involved in direct association with ML-SA1 include both polar and hydrophobic residues (Fig. 5*F*). Among these residues, I556 on S4, W380 in finger 2 of the TOP domain, and V655 on the loop between pore helix 2 (PH2) and S6 of a neighboring subunit may interact with ML-SA1 via Van der Waals effects. Q456 on the beta-sheet 5 (β5) of the TOP domain, Q557 and N560 on S4, and N653 in the pore loop of the neighboring subunit may also contribute to the binding of ML-SA1 (Fig. 5*F*).

The Binding of ML-SA1 at the TOP/Outer Pore Site May Lead to Partial Closure of the Ion-Conducting Pore. When comparing the previously published cryo-EM structures of the WT PC2 (21) and PC2_F604P_apo (27) with our structures PC2_F604P_lipid and PC2_F604P_ML-SA1, we noticed significant changes in the ion-conducting pore in PC2_F604P_ML-SA1 (Fig. 5*G*). The gate of the WT PC2, which was resolved in a closed state, is formed by L677 and N681 on S6, and the diagonal distance between the opposing L677 is 4.94 Å, suggesting a closed state (Fig. 5 *G*, *Left* panel) (21). In the PC2_F604P_apo structure, the F604P mutation-caused π-helix to α-helix transition in S6 and the rotation of the bottom half of S6 removes the side chains of L677 and N681 from the pore and opens the gate (27). The diagonal distance between the opposing F676, which forms the narrowest part in the pore, is 7.85 Å (Fig. 5 *G*, second panel from *Left*). In the structure of PC2_F604P_lipid, the α-helix in the middle of S6 stays the same as that in PC2_F604P_apo, and the diagonal distance between the opposing F676 is a similar 7.46 Å (Fig. 5 *G*, second panel from the *Right*). Compared to the structure of PC2_F604_apo, an extra helical turn down to E686 was resolved in the S6 of PC2_F604P_lipid (Fig. 5 *G* and *H*). This part of the pore remains open, and the diagonal distance between the opposing Y684 is 13.8 Å (Fig. 5*G*). In the case of PC2_F604P_ML-SA1, although its overall structure is like PC2_F604P_lipid, it has a narrower lower pore due to slightly shifted positions of some key side chains. The C terminus of S6 in the structure of PC2_F604P_ML-SA1 was resolved down to K688 (Fig. 5*H*), and the diagonal distance between the opposing F676 becomes a much shorter 5.88 Å, similar to that in the closed WT channel (Fig. 5 *G*, *Right* panel). More significantly, the diagonal distance at the narrowest part of the pore, which is formed by opposing Y684, is only 4.07 Å, (Fig. 5*G*). The pore radius plots of these four structures of PC2 also suggest that the narrower pore in PC2_F604P_ML-SA1 is less ion conductible compared to other PC2_F604P structures (Fig. 5*I*). Intriguingly, a similar intracellular gate closed by aromatic residues was also observed in the homologous PKD1L3/PKD2L1 channel (51). We hypothesize that the closed lower pore in PC2_F604P_ML-SA1 is caused by the binding of ML-SA1 at the TOP/outer pore site.

Meanwhile, the orientation shift of some side chains in the lower pore is the only significant change we found in the structure of the PC2_F604P_ML-SA1. The overall conformation of its pore helices (S5 and S6) is still very similar to that of the PC2_F604P_apo and PC2_F604P_lipid (Fig. 5*H*). Thus, the current structures may not provide a complete picture of the high-concentration ML-SA1-induced inactivation of the PC2_F604P channel. We hypothesize that the closed lower pore observed in the structure of the PC2_F604P_ML-SA1 is only part of the conformational changes happen during the high-concentration ML-SA1-induced inactivation, while the others were not resolved in the current structure.

The TOP/Outer Pore Binding of ML-SA1 Is Involved in the High-Concentration ML-SA1-Induced Inactivation. The closed pore observed in the structure of PC2_F604P_ML-SA1 suggests that the binding of ML-SA1 at the TOP/outer pore region may be involved in high-concentration ML-SA1-induced inactivation of PC2_F604P. To test this hypothesis, we made a series of mutations at this site and tested their effects in ML-SA1-induced activation and inactivation. In the PC2_F604P_ML-SA1 structure, the ML-SA1 binding cavity at the TOP/outer pore site is formed by three structural components: the β5 of the TOP domain, S4, and the loop between PH2 and S6 of a neighboring subunit (Fig. 6*A*). In our test, we picked some critical residues from each structural component and made the following seven mutations: Q456A, Q456W, Q557A, Q557W, N560A, N653A and N653T. To better describe the inhibitory effects of 100 μM ML-SA1 on PC2_F604P current, we divided the current of PC2_F604P after

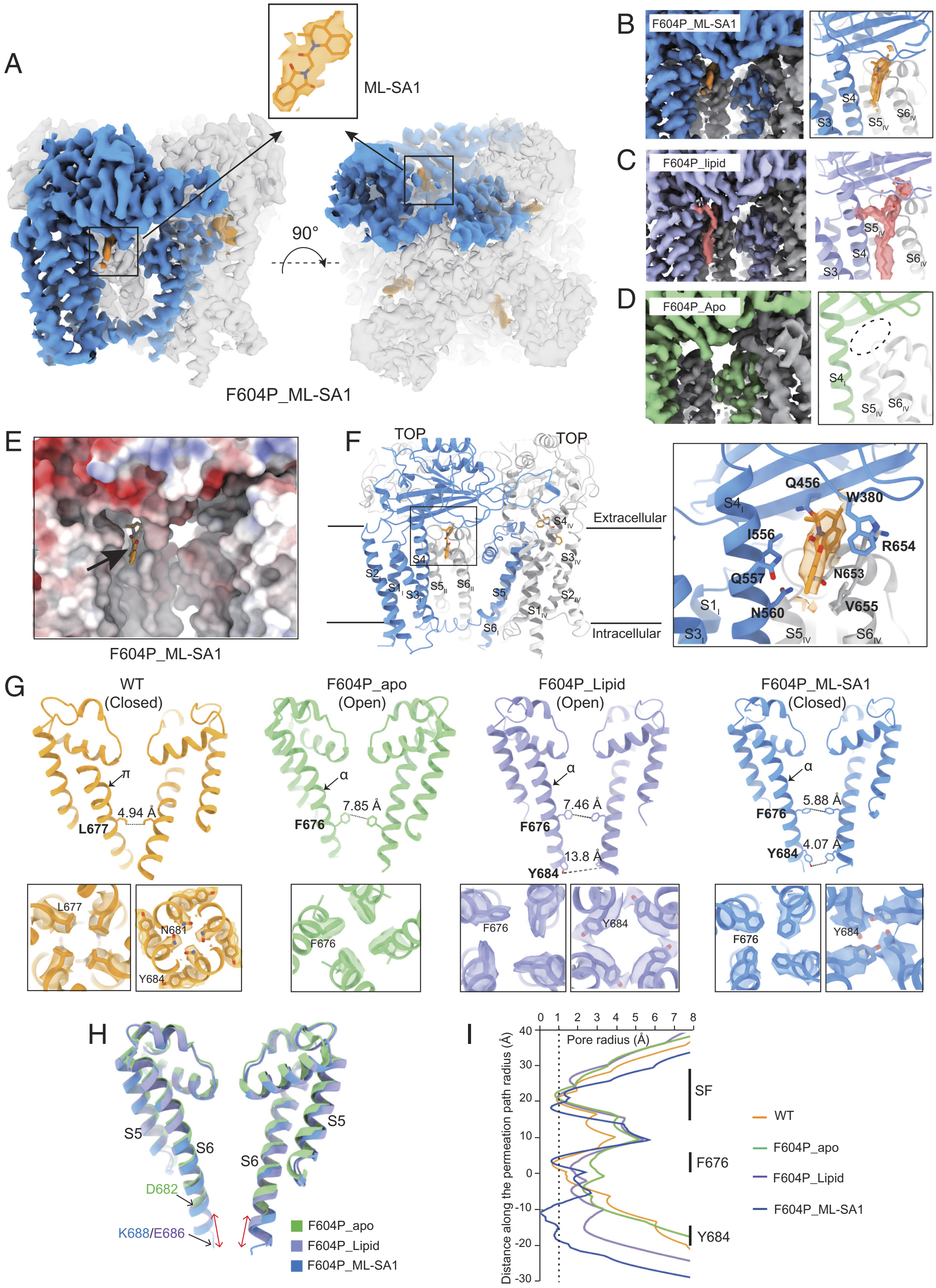

Fig. 5. Cryo-EM structures show that ML-SA1 binds at the TOP/outer pore site of PC2 and may lead to channel closing. (*A*) Two orthogonal surface views of cryo-EM reconstruction of PC2-F604P in the presence of 200 μM ML-SA1. The corresponding EM densities for ML-SA1 are in orange. One of them is highlighted within the boxes and shown in transparency on top. Structural figures were prepared in UCSF ChimeraX (49) if not otherwise indicated. (*B*–*D*) Close-up views of the density maps (*Left*) and cartoon (*Right*) of 3D reconstructions of PC2-F604P in ML-SA1-bound (blue, *B*) and lipid-bound (purple, *C*) state, compared to PC2-F604P apo structure reported previously (27) (green, *D*, PDB code: 6D1W). The EM densities corresponding to the lipid (pink) and ML-SA1 (orange) are represented in transparency in the cartoon view. All the maps are contoured at 4σ. The EM maps shown in this manuscript are under C4 symmetry unless otherwise indicated. (*E*) Close-up views of the electrostatic potential surface of the ML-SA1 binding site, calculated by coulombic electrostatic potential in ChimeraX (49), coloring ranging from red for negative potential through white to blue for positive potential. ML-SA1 is indicated by a black arrow. (*F*) Cartoon shows that ML-SA1 binds to the TOP/outer pore site. The detailed interaction interface between ML-SA1 and PC2_F604P is shown in the *Right* panel. The key side chains that may be involved in binding are represented in sticks. R654 in the outer pore is also labeled to indicate its cation-pi interaction with W380 in the TOP domain. (*G*) TOP: Side views of the ion permeation pathway of two opposing subunits for the PC2 WT [orange, PDB code: 5Z1W (21)], PC2-F604P_apo [green, PDB code: 6D1W (27)], PC2-F604P_lipid (purple) and PC2-F604P_ML-SA1 (blue) structures. A π-helix in the middle of S6 in the WT PC2, which is transited to α-helix in other structures, is indicated. The key residues that form major constrictions in the pore are shown in sticks and the diagonal distances in Å between opposing residues are labeled. The corresponding EM densities for these residues are highlighted within the black boxes at the bottom. (*H*) Superimposing the pore domain of F604P_apo (green), F604P_lipid (purple), and F604P_mL-SA1 (blue) structures. The elongated intracellular gates in both F604P_lipid and F604P_ML-SA1 structures are indicated by red arrows. (*I*) Comparison of pore radii in structures shown in *G*, which are calculated using the HOLE program (50). The dotted line denotes a 1.0 Å-radius.

the application of 100 ML-SA1 ($I_{100\ \mu M\ ML\text{-}SA1}$) for 2 min by the current after the application of 20 μM ML-SA1 ($I_{20\ \mu M\ ML\text{-}SA1}$) for about 10 s and named the ratio "inactivation index." Plotting the inactivation index of each oocyte allows us to measure how 100 μM ML-SA1 leads to the inactivation of the 20 μM ML-SA1-activated PC2_F604P (Fig. 6*C*). Within the seven mutations, the last two mutations on the pore loop, N653A and N653T, led to complete loss of the PC2_F604P channel activity (*SI Appendix*, Fig. S10), suggesting that N653 is critical for the function of PC2. The effects of ML-SA1 on three other mutations, Q456A, Q557W, and N560A, are roughly the same as the PC2_F604P channel: applying 20 μM quickly doubled the channel current while applying 100 μM inhibited current (Fig. 6*C* and *SI Appendix*, Fig. S11). However, in the cases of mutant Q456W and Q557A, although they have normal ML-SA1 activation as PC2_F604P, their inactivation by 100 μM ML-SA1 is significantly smaller (Fig. 6 *B* and *C*). Especially in the case of Q557A, the inactivation was almost abolished. Instead of causing inactivation, applying 100 μM ML-SA1 further activated this mutant in most of the tested oocytes (Fig. 6 *B* and *C*). These results strongly suggest that the high concentration ML-SA1-induced inactivation of PC2_F604P is caused by its binding to the TOP/outer pore site shown in the cryo-EM structure.

The fact that Q557A and Q456W only affected the high-concentration ML-SA1-induced inactivation but did not change low-concentration ML-SA1-induced activation (Fig. 6 *B* and *C*) further proves that the latter is via binding of ML-SA1 at another site. The reason that we do not see ML-SA1 in the higher affinity activation site (S5-PH1-S6) in our cryo-EM structure is unknown. Besides of the possible high flexibility of ML-SA1 at this site, another unproved possibility is that the second binding at the TOP/outer pore site leads to dissociation of ML-SA1 from the S5-PH1-S6 site, as part of the inhibitory mechanism.

Applying 100 μM of SF-71, one of the channel inhibitors we found in this study, caused more inhibition of the channel activity compared to 20 μM (Fig. 6 *D*, *Left*). This trend was not changed by the mutation Q557A (Fig. 6 *D*, *Right*), suggesting SF-71 may not bind to the same TOP/outer pore site as ML-SA1. We assume that its inhibitory effect is solely from the binding to the S5-PH1-S6 site as described above.

Based on our cryo-EM structures and the mutagenesis results, we generated a working model of the dual regulation of PC2_F604P by ML-SA1 (Fig. 7). At lower concentrations (<20 μM), ML-SA1 binds to the S5-PH1-S6 site and further activates the PC2_F604P channel. The channel gains weak permeability of Ca^{2+} after ML-SA1 activation (Fig. 7 *A* and *B*). At higher concentrations (>20 μM), ML-SA1 further binds to the TOP/outer pore site and causes inactivation of the PC2_F604P channel. The conformational changes in the inactivation may include the closing of the lower pore (Fig. 7*C*).

We have also tested some of these small molecules on the heteromeric PC1/PC2 channel. Similar to that on the WT PC2 and PC2_AA, 20 μM ML-SA1, SF-51, SF-33, and SF-71 showed no obvious effect on a truncated PC1/PC2 and the GOF PC1/PC2_AA mutant channels (*SI Appendix*, Fig. S12 *A* and *B*) (9). Interestingly, in contrast to that on PC2_F604P, we did not observe significant effects of these molecules on the GOF PC1/PC2_F604P channel (*SI Appendix*, Fig. S12*C*). The structure of PC2 subunits is highly conserved in the homomeric and heteromeric channels (10, 21). If these molecules still bind to PC2 subunits in PC1/PC2_F604P, our results suggest that the two types of channels may have distinct gating mechanisms.

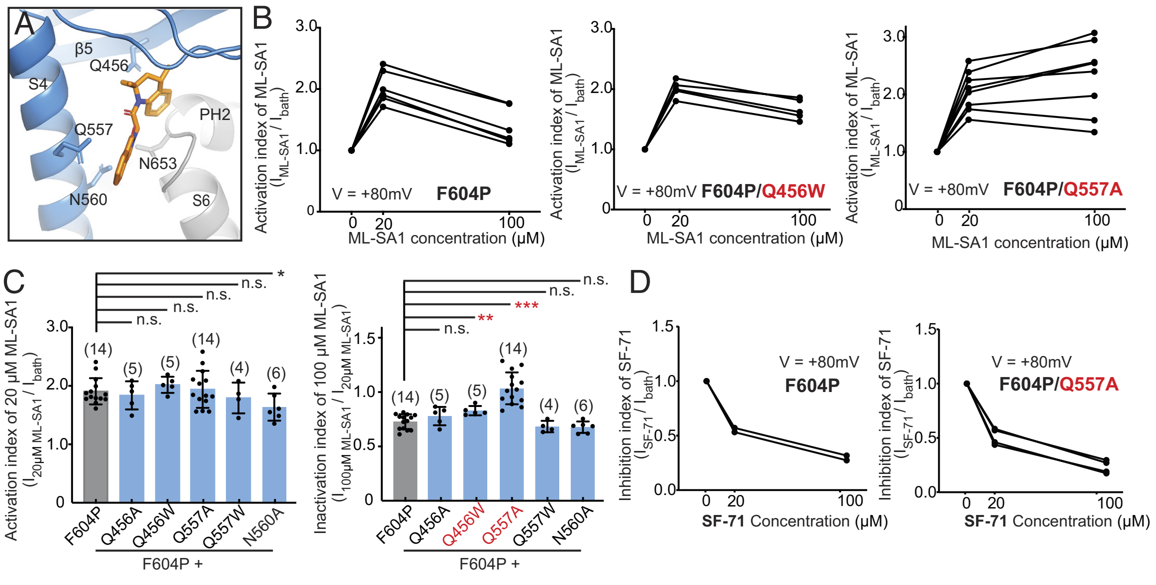

Fig. 6. Mutations at the TOP/outer pore site reduce/abolish the high concentration ML-SA1-induced inhibition of PC2_F604P. (*A*) Detailed structure of PC2_F604P_ML-SA1 shows the key residues contribute to the ML-SA1 binding at the TOP/outer pore site. ML-SA1 is shown in orange. This structural image was prepared with PyMOL (The Pymol Molecular Graphics System). (*B*) Plots of the activation index of ML-SA1 at 20 and 100 μM from individual oocytes expressing the PC2_F604P, PC2_F604P/Q456W, or PC2_F604P/Q557A, showing the Q456W and Q557A mutations led to a reduced inhibition of 100 μM ML-SA1. Data of 100 μM were collected after 2 min ML-SA1 application. Results of the other tested mutants are included in *SI Appendix*, Fig. S11. (*C*) Scatter plot and bar graphs show the activation index of 20 μM ML-SA1 (*Left*) and the inactivation index of 100 μM ML-SA1 (ratio of current at +80 mV after 100 μM ML-SA1 was applied for 2 min vs. current after 20 μM ML-SA1 was applied for 10 to 15 s, $I_{100\ \mu M\ ML\text{-}SA1}/I_{20\ \mu M\ ML\text{-}SA1}$) (*Right*) of PC2_F604P and the indicated mutants. Oocyte numbers are indicated in parentheses. Data are presented as mean ± SD (n.s.: not significant, $^{**}P < 0.01$, $^{***}P < 0.001$, Student's *t* test). (*D*) Plots of the inhibition index of SF-71 (ratio of current after SF-71 application vs. current before application) at 20 and 100 μM when applied to PC2_F604P and the Q557A mutant, showing no change caused by Q557A mutation. Data of 100 μM were collected after 2 min SF-71 application.

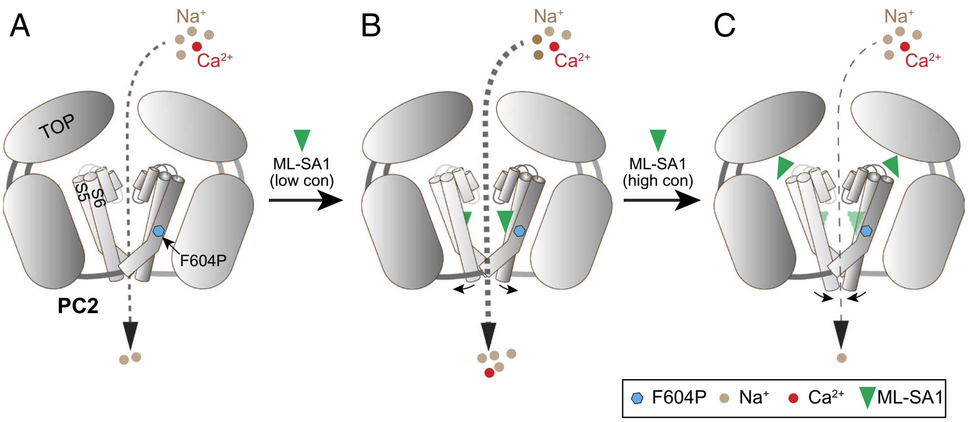

Fig. 7. A working model of the dual regulation of PC2_F604P by ML-SA1. (*A*) PC2_F604P is a GOF mutant that conducts Na^+ (brown dots) influx but is not permeable to Ca^{2+} (red dot). (*B*) ML-SA1 (green triangle) at low concentration (<20 μM) binds to the S5-PH1-S6 site and further activates the PC2_F604P channel. The ML-SA1-activated channel gain weak permeability of Ca^{2+}. (*C*) ML-SA1 at higher concentration (>20 μM) further binds to the TOP/outer pore site and causes inactivation of the PC2_F604P channel. The conformation changes in the inactivation may include the closing of the lower pore.

Discussion

In this study, we found two TRPML agonists, ML-SA1 and SF-51, further activate the GOF PC2_F604P channel (*SI Appendix*, Table S2). Combining the results from different approaches, we conclude that ML-SA1 has two binding sites in PC2_F604P that have different binding affinities. The first one that aligns to the S5-PH1-S6 binding site of ML-SA1 in TRPML channels has higher affinity and ML-SA1-binding here further activates PC2_F604P (Fig. 2). Most of the residues involved in forming this binding site are conserved among TRPP proteins and between the TRPP and TRPML families (Fig. 2). Although this ML-SA1 molecule binding was not resolved in our structures, the mutagenesis and the molecular docking results, strongly suggest that the binding of ML-SA1 here, and the involvement of this binding in ML-SA1-induced activation of PC2_F604P (Fig. 2). Our data also suggest that the binding site is shared by some inhibitors of PC2_F604P identified in this study (Fig. 3). Shared binding sites between agonists and antagonists are seen in other TRP channels. For example, in TRPV channels, the vanilloid agonist-binding site was found to also bind inhibitors such as capsazepine in TRPV1 and cis22a in TRPV6 (33).

We further showed that the second binding site of ML-SA1 in PC2_F604P is formed by the TOP domain, the S4, and the outer pore region of a neighboring subunit. This site has a lower affinity and is only occupied when ML-SA1 concentration is higher than >20 μM (Fig. 4*E*). Binding of ML-SA1 at this site leads to the inactivation of the channel (Figs. 4–6), which is supported by the cryo-EM structure (Fig. 5) and the mutagenesis results (Fig. 6). Since the outer pore region is involved in defining the conformations of the pore and the selectivity filter, it is reasonable that ML-SA1 binding here directly regulates channel function. Among the residues that are involved in this binding, Q557 and R654 are conserved in PC2 and PC2L1, while W380, Q456, N560, N653, and V655 are conserved in all three TRPP members (PC2, PC2L1, and PC2L2). Considering the structures of PC2 and PC2L1 also share high similarity (19–21, 31, 32), it is possible that ML-SA1 also binds to similar sites in the other two TRPP proteins. On the other hand, these residues and the local structure of the TOP/outer pore binding site are not conserved in TRPML channels. Thus, we hypothesize that ML-SA1 does not bind to TRPML channels at this site. Consistently, there is no report about inactivating TRPML channels by ML-SA1.

Thus, significantly, we found that ML-SA1 binds at two sites in PC2_F604P, and each binding leads to distinct effects on PC2_F604P function. This dual regulation is also given by SF-51, another agonist found in this study (Fig. 4). Previously, Ca^{2+} has been found to have dual effects on PC2 channel function. Applying Ca^{2+} less than micromolar concentrations on the cytoplasmic side increased the channel activity, but a higher concentration of Ca^{2+} led to inhibition instead (12, 52, 53). These concentration-dependent effects suggest that they are carried out by Ca^{2+} binding to more than one site with different binding affinities. Dual regulations from the same factor have also been observed in other membrane proteins. For example, Zn^{2+} was found to both inhibit and activate the Otop1 and Otop3 proton channels, and the two effects were done by Zn^{2+} binding at distinct sites (54).

In the structure of PC2_F604P_lipid, we observed a lipid molecule binds at almost the same binding site as ML-SA1 (Fig. 5 *A* and *B*). Interestingly, this site is close to but distinct from a phosphatidic acid (PA) binding site in a previously reported cryo-EM structure of the WT PC2 (19). Our results suggest that when a high concentration (>20 μM) of ML-SA1 is present, ML-SA1 will compete off the lipid binding to inactivate the channel. A similar situation was observed in the vanilloid-binding site in TRPV channels (33). In the absence of an agonist, this site is occupied by lipid molecules [phosphatidylinositol (PI) in the case of TRPV1]. Since the other agonists have to compete off the lipid from this site to activate particular TRPV channels, these lipid molecules can also be considered endogenous inhibitors of the channels (33). It will be interesting to investigate whether lipid binding at the TOP/outer pore site modulates PC2 channel function.

Although we did not observe the effect on the WT PC2 channel in our initial screen with all tested small molecules (*SI Appendix*, Table S2 and Fig. S3), we could not rule out the possibility that ML-SA1 or other molecules bind to WT PC2, but the effect is not strong enough to open the channel. Meanwhile, if the effect is inhibitory, we will also not be able to record the change since WT PC2 was in a closed state in our test. Based on the high conservation of both the sequence and structure of the S5-PH1-S6 binding site, it is reasonable to suspect that some of these molecules may be able to bind there in WT PC2. The structure of the TOP/outer pore site is also similar between the WT and the F604P mutant of PC2. Thus, ML-SA1 may also bind to the closed or naturally gated PC2 at this site to regulate its channel function. More work is needed to investigate how some of these ligands may bind and regulate the WT PC2 channel. It is worth noting that here we did our test on PC2 expressed in *Xenopus* oocytes. If possible, it will be valuable to test these molecules with mammalian cell–expressed PC2, although we had challenges in this approach since overexpressed PC2 tends to stay in the ER membrane in these cells (55).

The fact that these ligands further activate the opened GOF channel suggests a possibility that naturally gated PC2 channel can also be further activated by these ligands. Meanwhile, it indicates that either the F604P mutation only leads to partial opening of the gate, which can be further opened by ligand-binding, or that the PC2 channel can have different open states responding to different stimuli. TRP channels are well known to be regulated by multiple stimuli or ligands, and their activations are polymodal (56). A good example is the founding member of the TRPV channel subfamily, TRPV1. As a thermo-TRP channel, TRPV1 can be activated by hot temperature (14). At the same time, the channel can also be activated by multiple agonists, such as capsaicin, resiniferatoxin (RTX), and double-knot toxin (DkTx), etc. (33). These agonists can bind to varied sites in the TRPV1 structure and lead to different open states of the channel, and the ligand-induced gating is also distinct from the temperature-induced gating (33, 57, 58). Thus, it is not surprising if PC2 also has distinct open states responding to different stimuli and some stimuli have superimposed effect on channel gating.

The dual regulatory effects of small-molecular ligands of PC2 observed in this study showcase the complexity of interactions between ligands and ion channels. Our study also shows that TRPP and TRPML channels have shared small-molecule ligands due to their sequence and structural similarity. Thus, caution needs to be taken when applying these molecules to study the in vivo functions of these channels and to treat related diseases. At the same time, the identification of ML-SA1 and SF-51 as ligands of PC2_F604P provides a chemical scaffold for generating molecules that can more efficiently regulate the PC2 channel.

Material and Methods

cDNA Constructs. Human PKD2 cDNAs (NCBI accession no. U50928) were used for functional study, and a truncated human construct, encoding PC2 amino acids from Pro185 to Lys719, was used for structure determination.

Electrophysiology. RNAs were synthesized in vitro and injected into *X. laevis* oocytes (30 ng RNA/oocyte). The two-electrode voltage clamp (TEVC) method was used to record whole-oocyte currents.

In Silico Docking. AutoDock 4.2 (59) was used to dock ML-SA1 into the potential binding sites of PC2_F604P.

Cryo-EM Sample Preparation, Data Collection and Processing, and Model Building. PC2_F604P were expressed in HEK293expi cells and purified with affinity pull-down and size-exclusion chromatography. A Titan Krios electron microscope (Thermo Fisher) was used for EM data collection. EM particles were picked, and 2D classification, 3D global classification, and 3D auto-refinement using C4 symmetry were performed. The coordinates of the human PC2 structure (PDB code: 6D1W) were used as the initial model.

Other Materials and Methods. Details for the methods described above are provided in *SI Appendix*, *Supporting Text*.

Data, Materials, and Software Availability. The atomic coordinates and EM maps for the PC2_F604P_Lipid and PC2_F604P_ML-SA1 have been deposited to PDB with the accession codes 8K3S (60) and 8HK7 (61), and EMDB with the codes EMD-36858 (62) and EMD-34848 (63), respectively.

ACKNOWLEDGMENTS. We thank Xiaojuan Wang at the cryo-EM facility of Westlake University, and the High-Performance Computing Center, and the Mass Spectrometry & Metabolomics Core Facility of Westlake University for facility support and technical assistance. We thank members of Yu lab and Shi lab for commenting on the manuscript. This work was supported by grants from NIH (R01DK125404 to Y.Y. and F.Q.), National Natural Science Foundation of China (31930059 and 81920108015 to Y.S.), and National Key R&D Program of China (2020YFA050930 to Y.S.).

Author affiliations: [a]Department of Biological Sciences, St. John's University, Queens, NY 11375; [b]Research Center for Industries of the Future, Key Laboratory of Structural Biology of Zhejiang Province, School of Life Sciences, Westlake University, Hangzhou, Zhejiang province 310024, China; [c]Westlake Laboratory of Life Sciences and Biomedicine, Institute of Biology, Westlake Institute for Advanced Study, Hangzhou, Zhejiang province 310024, China; [d]Beijing Frontier Research Center for Biological Structures, Tsinghua-Peking Joint Center for Life Sciences, School of Life Sciences, Tsinghua University, Beijing 100084, China; and [e]Division of Nephrology, Department of Medicine, University of Maryland School of Medicine, Baltimore, MD 21201

1. P. C. Harris, V. E. Torres, Polycystic kidney disease. *Annu. Rev. Med.* **60**, 321–337 (2009).
2. G. Wu, S. Somlo, Molecular genetics and mechanism of autosomal dominant polycystic kidney disease. *Mol. Genet Metab.* **69**, 1–15 (2000).
3. J. Zhou, Polycystins and primary cilia: Primers for cell cycle progression. *Annu. Rev. Physiol.* **71**, 83–113 (2009).
4. M. Semmo, M. Kottgen, A. Hofherr, The TRPP subfamily and polycystin-1 proteins. *Handb. Exp. Pharmacol.* **222**, 675–711 (2014).
5. L. Tsiokas, E. Kim, T. Arnould, V. P. Sukhatme, G. Walz, Homo- and heterodimeric interactions between the gene products of PKD1 and PKD2. *Proc. Natl. Acad. Sci. U.S.A.* **94**, 6965–6970 (1997).
6. F. Qian *et al.*, PKD1 interacts with PKD2 through a probable coiled-coil domain. *Nat. Genet.* **16**, 179–183 (1997).
7. Z. Salehi-Najafabadi *et al.*, Extracellular loops are essential for the assembly and function of polycystin receptor-ion channel complexes. *J. Biol. Chem.* **292**, 4210–4221 (2017).
8. Y. Yu *et al.*, Structural and molecular basis of the assembly of the TRPP2/PKD1 complex. *Proc. Natl. Acad. Sci. U.S.A.* **106**, 11558–11563 (2009).
9. Z. Wang *et al.*, The ion channel function of polycystin-1 in the polycystin-1/polycystin-2 complex. *EMBO Rep.* **20**, e48336 (2019).
10. Q. Su *et al.*, Structure of the human PKD1-PKD2 complex. *Science* **361**, eaat9819 (2018).
11. K. Hanaoka *et al.*, Co-assembly of polycystin-1 and -2 produces unique cation-permeable currents. *Nature* **408**, 990–994 (2000).
12. P. Koulen *et al.*, Polycystin-2 is an intracellular calcium release channel. *Nat. Cell Biol.* **4**, 191–197 (2002).
13. S. Gonzalez-Perrett *et al.*, Polycystin-2, the protein mutated in autosomal dominant polycystic kidney disease (ADPKD), is a Ca2+-permeable nonselective cation channel. *Proc. Natl. Acad. Sci. U.S.A.* **98**, 1182–1187 (2001).
14. C. Montell, The TRP superfamily of cation channels. 2005, re3 (2005).
15. D. E. Clapham, TRP channels as cellular sensors. *Nature* **426**, 517–524 (2003).
16. B. Nilius, G. Owsianik, T. Voets, J. A. Peters, Transient receptor potential cation channels in disease. *Physiol. Rev.* **87**, 165–217 (2007).
17. M. M. Moran, M. A. McAlexander, T. Biro, A. Szallasi, Transient receptor potential channels as therapeutic targets. *Nat. Rev. Drug Discov.* **10**, 601–620 (2011).
18. E. Cao, Structural mechanisms of transient receptor potential ion channels. *J. Gen. Physiol.* **152**, e201811998 (2020).
19. M. Wilkes *et al.*, Molecular insights into lipid-assisted Ca(2+) regulation of the TRP channel Polycystin-2. *Nat. Struct. Mol. Biol.* **24**, 123–130 (2017).
20. M. Grieben *et al.*, Structure of the polycystic kidney disease TRP channel Polycystin-2 (PC2). *Nat. Struct. Mol. Biol.* **24**, 114–122 (2017).
21. P. S. Shen *et al.*, The structure of the polycystic kidney disease channel PKD2 in lipid nanodiscs. *Cell* **167**, 763–773.e711 (2016).
22. X. Zhou *et al.*, Cryo-EM structures of the human endolysosomal TRPML3 channel in three distinct states. *Nat. Struct. Mol. Biol.* **24**, 1146–1154 (2017).
23. P. Schmiege, M. Fine, G. Blobel, X. Li, Human TRPML1 channel structures in open and closed conformations. *Nature* **550**, 366–370 (2017).
24. M. Hirschi *et al.*, Cryo-electron microscopy structure of the lysosomal calcium-permeable channel TRPML3. *Nature* **550**, 411–414 (2017).
25. Q. Chen *et al.*, Structure of mammalian endolysosomal TRPML1 channel in nanodiscs. *Nature* **550**, 415–418 (2017).
26. M. Li *et al.*, Structural basis of dual Ca(2+)/pH regulation of the endolysosomal TRPML1 channel. *Nat. Struct. Mol. Biol.* **24**, 205–213 (2017).
27. W. Zheng *et al.*, Hydrophobic pore gates regulate ion permeation in polycystic kidney disease 2 and 2L1 channels. *Nat. Commun.* **9**, 2302 (2018).
28. M. Arif Pavel *et al.*, Function and regulation of TRPP2 ion channel revealed by a gain-of-function mutant. *Proc. Natl. Acad. Sci. U.S.A.* **113**, E2363–2372 (2016).
29. Y. Wang *et al.*, The diverse effects of pathogenic point mutations on ion channel activity of a gain-of-function polycystin-2. *J. Biol. Chem.* **299**, 104674 (2023).
30. K. Ha *et al.*, The heteromeric PC-1/PC-2 polycystin complex is activated by the PC-1 N-terminus. *eLife* **9**, e60684 (2020).
31. Q. Su *et al.*, Cryo-EM structure of the polycystic kidney disease-like channel PKD2L1. *Nat. Commun.* **9**, 1192 (2018).
32. R. E. Hulse, Z. Li, R. K. Huang, J. Zhang, D. E. Clapham, Cryo-EM structure of the polycystin 2–l1 ion channel. *eLife* **7**, e36931 (2018).
33. M. V. Yelshanskaya, A. I. Sobolevsky, Ligand-binding sites in vanilloid-subtype TRP channels. *Front. Pharmacol.* **13**, 900623 (2022).

34. Q. Wang *et al.*, Lipid interactions of a ciliary membrane TRP channel: Simulation and structural studies of polycystin-2. *Structure* **28**, 169–184.e165 (2020).
35. D. Shen *et al.*, Lipid storage disorders block lysosomal trafficking by inhibiting a TRP channel and lysosomal calcium release. *Nat. Commun.* **3**, 731 (2012).
36. C. Grimm *et al.*, Small molecule activators of TRPML3. *Chem. Biol.* **17**, 135–148 (2010).
37. E. Plesch *et al.*, Selective agonist of TRPML2 reveals direct role in chemokine release from innate immune cells. *eLife* **7**, e39720 (2018).
38. C. C. Chen *et al.*, A small molecule restores function to TRPML1 mutant isoforms responsible for mucolipidosis type IV. *Nat. Commun.* **5**, 4681 (2014).
39. X. Liu *et al.*, Polycystin-2 is an essential ion channel subunit in the primary cilium of the renal collecting duct epithelium. *eLife* **7**, e33183 (2018).
40. S. J. Kleene, N. K. Kleene, The native TRPP2-dependent channel of murine renal primary cilia. *Am. J. Physiol. Renal Physiol.* **312**, F96–F108 (2017).
41. B. C. Schroeder, T. Cheng, Y. N. Jan, L. Y. Jan, Expression cloning of TMEM16A as a calcium-activated chloride channel subunit. *Cell* **134**, 1019–1029 (2008).
42. Y. D. Yang *et al.*, TMEM16A confers receptor-activated calcium-dependent chloride conductance. *Nature* **455**, 1210–1215 (2008).
43. A. Caputo *et al.*, TMEM16A, a membrane protein associated with calcium-dependent chloride channel activity. *Science* **322**, 590–594 (2008).
44. N. Gan *et al.*, Structural mechanism of allosteric activation of TRPML1 by PI(3,5)P(2) and rapamycin. *Proc. Natl. Acad. Sci. U.S.A.* **119**, e2120404119 (2022).
45. M. Fine, P. Schmiege, X. Li, Structural basis for PtdInsP(2)-mediated human TRPML1 regulation. *Nat. Commun.* **9**, 4192 (2018).
46. P. Schmiege, M. Fine, X. Li, Atomic insights into ML-SI3 mediated human TRPML1 inhibition. *Structure* **29**, 1295–1302.e1293 (2021).
47. Y. Gao, E. Cao, D. Julius, Y. Cheng, TRPV1 structures in nanodiscs reveal mechanisms of ligand and lipid action. *Nature* **534**, 347–351 (2016).
48. L. Tang *et al.*, Structural basis for inhibition of a voltage-gated Ca(2+) channel by Ca(2+) antagonist drugs. *Nature* **537**, 117–121 (2016).
49. E. F. Pettersen *et al.*, UCSF ChimeraX: Structure visualization for researchers, educators, and developers. *Protein Sci.* **30**, 70–82 (2021).
50. O. S. Smart, J. G. Neduvelil, X. Wang, B. A. Wallace, M. S. Sansom, HOLE: A program for the analysis of the pore dimensions of ion channel structural models. *J. Mol. Graph* **14**, 354–360 (1996).
51. Q. Su *et al.*, Structural basis for Ca(2+) activation of the heteromeric PKD1L3/PKD2L1 channel. *Nat. Commun.* **12**, 4871 (2021).
52. P. M. Vassilev *et al.*, Polycystin-2 is a novel cation channel implicated in defective intracellular Ca(2+) homeostasis in polycystic kidney disease. *Biochem. Biophys. Res. Commun.* **282**, 341–350 (2001).
53. Y. Cai *et al.*, Calcium dependence of polycystin-2 channel activity is modulated by phosphorylation at Ser812. *J. Biol. Chem.* **279**, 19987–19995 (2004).
54. B. Teng *et al.*, Zinc activation of OTOP proton channels identifies structural elements of the gating apparatus. *eLife* **12**, e85317 (2023).
55. Y. Cai *et al.*, Identification and characterization of polycystin-2, the PKD2 gene product. *J. Biol. Chem.* **274**, 28557–28565 (1999).
56. I. S. Ramsey, M. Delling, D. E. Clapham, An introduction to TRP channels. *Annu. Rev. Physiol.* **68**, 619–647 (2006).
57. D. H. Kwon *et al.*, Heat-dependent opening of TRPV1 in the presence of capsaicin. *Nat. Struct. Mol. Biol.* **28**, 554–563 (2021).
58. E. Cao, M. Liao, Y. Cheng, D. Julius, TRPV1 structures in distinct conformations reveal activation mechanisms. *Nature* **504**, 113–118 (2013).
59. G. M. Morris *et al.*, AutoDock4 and AutoDockTools4: Automated docking with selective receptor flexibility. *J. Comput. Chem.* **30**, 2785–2791 (2009).
60. M. Chen, Q. Su, Z. Wang, Y. Yu, 8K3S, Structure of PKD2-F604P complex. Protein Data Bank. https://www.rcsb.org/structure/8K3S. Deposited 24 July 2023.
61. M. Chen, Q. Su, Z. Wang, Y. Yu, 8HK7, Structure of PKD2-F604P (Polycystin-2, TRPP2) with ML-SA1. Protein Data Bank. https://www.rcsb.org/structure/8HK7. Deposited 28 November 2022.
62. M. Chen, Q. Su, Z. Wang, Y. Yu, EMD-36858, Structure of PKD2-F604P complex. Electron Microscopy Database. https://www.ebi.ac.uk/emdb/EMD-36858. Deposited 24 July 2023.
63. M. Chen, Q. Su, Z. Wang, Y. Yu, EMD-34848, Structure of PKD2-F604P (Polycystin-2, TRPP2) with ML-SA1. Electron Microscopy Database. https://www.ebi.ac.uk/emdb/EMD-34848. Deposited 28 November 2022.